Results in Physics 56 (2024) 107236

Contents lists available at ScienceDirect

Results in Physics

journal homepage: www.elsevier.com/locate/rinp

Two-qubit entangling gates for superconducting quantum computers

Muhammad AbuGhanem [a,b,*], Hichem Eleuch [c,d,e]

[a] Faculty of Science, Ain Shams University, Cairo, 11566, Egypt
[b] Zewail City of Science, Technology and Innovation, Giza, 12678, Egypt
[c] Department of Applied Physics and Astronomy, University of Sharjah, 27272 Sharjah, United Arab Emirates
[d] College of Arts and Sciences, Abu Dhabi University, Abu Dhabi 59911, United Arab Emirates
[e] Institute for Quantum Science and Engineering, Texas A&M University, College Station, TX 77843, USA

ARTICLE INFO

Keywords:
Entangling gates
Dagwood Bumstead gate
Quantum state tomography
Quantum process tomography
Novel two-qubit quantum gates
IBM's NISQ quantum computers

ABSTRACT

Noisy intermediate-scale quantum computers (NISQ) have demonstrated superior performance compared to conventional computing schemes. Nonetheless, errors associated with two-qubit entangling gates remain a substantial obstacle in fully harnessing the potential of current superconducting quantum computers. The achievement of quantum computation and quantum information processing critically depends on the presence of entangled states. These states are indispensable for quantum computers to surpass classical computers in terms of computational power. This paper presents a comprehensive characterization of a two-qubit entangling gate, known as Dagwood Bumstead (DB) gate, to investigate the challenges posed by errors in the DB gate on NISQ devices. Firstly, we propose a scheme for the realization of the DB gate using two capacitively coupled Josephson Superconducting qubits, based on the experimental setup carried out in Bialczak et al. (2010). Additionally, we introduce and characterize a novel two-qubit quantum gate. Our proposed gate showcases an impressive average gate fidelity of 0.85450. The DB gate's performance is fully described through quantum process tomography (QPT) and quantum state tomography (QST) experiments conducted in three different environments: noisy, noiseless, and on a real IBM quantum computer. The process fidelity of the DB gate is measured to be 0.8069705, and the state fidelity is determined to be 0.8858750. This study offers valuable insights into the performance of the DB gate on a NISQ device, showcasing its potential for executing intricate algorithms and operations on an authentic quantum computer.

Introduction

Quantum computing has emerged as a groundbreaking technology that could potentially solve problems that are currently intractable for classical computers. Scaling up quantum processors has advanced significantly [1] in recent years, with multiple implementations showing 54 [2] or more qubits (433) at different phases of development [3,4]. However, in order to fully benefit from growing qubit counts in noisy intermediate-scale quantum computers (NISQ) [5], the error rates of these processors must be limited proportionally.

To fully exploit the efficiency of quantum computing and quantum information processing, entangled states are required [6,7]. However, deficiencies in operating the two-qubit entangling gates are the principal inputs of error in the state-of-the-art quantum computing artificial architectures, such as trapped ions and superconducting qubit [8]. The implementation of scalable quantum computing architectures presents several challenges [9], particularly in gate implementation [9–14]. To address these challenges, researchers have explored various physical architectures. One of the most promising artificial architectures that could support scalable quantum computation on a solid-state platform is Superconducting qubits [15].

While many physical implementations of quantum computers exist [16–23], the Superconducting qubits based on Josephson junctions has garnered significant attention due to its advantages [24]. Superconducting (SC) qubits [25,26] are a highly promising platform for practical quantum computing systems. Their scalability on a solid-state platform [15], long coherence times, high fidelity, flexibility, and compatibility with classical electronics make them a preferred choice [24,26,27] for researchers and quantum computing manufacturing companies. SC qubits can be manufactured using standard semiconductor fabrication techniques, which makes them highly scalable for large-scale quantum computing systems. The coherence times of Superconducting qubits are relatively long, making them resistant to the decoherence phenomena that can be detrimental to quantum computations. Additionally, they are designed with high fidelity, with low

* Corresponding author at: Faculty of Science, Ain Shams University, Cairo, 11566, Egypt.
E-mail address: gaa1nem@gmail.com (M. AbuGhanem).

https://doi.org/10.1016/j.rinp.2023.107236
Received 1 July 2023; Received in revised form 23 November 2023; Accepted 29 November 2023
Available online 2 December 2023

error rates for quantum operations and measurements, making them an excellent choice for quantum computations [28,29]. SC qubits are flexible and can be reconfigured and controlled with external electromagnetic fields, providing the flexibility to design and implement various quantum algorithms. Finally, they are compatible with classical electronic circuits, facilitating efficient control and readout of qubit states [26]. Nevertheless, there are still significant challenges to overcome, such as improving the coherence times of qubits and reducing error rates for quantum operations.

Two-qubit gates are extremely difficult to achieve with High-fidelities. Furthermore, experimental implementations of such high-fidelity quantum gates is a crucial task in varied quantum systems [2]. To realize a universal quantum computer [30–32], a set of quantum gates is required [33,34], including two-qubit entangling gates [35,36]. The successful implementation of these gates is a critical milestone in the development of practical quantum computers [6]. One of the key challenges in developing a scalable quantum computer with Superconducting qubits is executing high-fidelity, 2-qubit quantum gates among an architecture that contains numerous resonant elements. The frequency space of the design becomes crowded as the number of elements in the architecture increases, or the variety of couplings between them rises, which has an adverse effect on device performance.

The two-qubit entangling gate is particularly essential, as it allows for the creation of entangled states, which are necessary for quantum computations that cannot be simulated efficiently on classical computers. Many approaches have been proposed for implementing two-qubit (entangling) gates in architectures composed of Superconducting qubits [37]. One approach uses fixed-frequency qubits with static couplings, where 2-qubit operations are energized by employing transverse microwave drives [38–44]. However, such architectures require stringent constraints on anharmonicities and qubit frequencies, which can limit scalability [42–44].

Another approach employs frequency-tunable qubits, and 2-qubit gates are made active by tuning qubits in- and out- of resonance with a certain transition [45–51]. While this approach offers scalability, it occurs at the expense of more decoherence channels, which significantly limits coherence times [52]. Additionally, it is challenging to deliver shaped unbalanced control signals in this approach, and unwanted crossings with neighboring qubit energy levels all along gate operations can limit the connectivity and flexibility of this architecture.

An alternate of these techniques is to regulate the couplings or energy levels of a circuit at a frequency that corresponds to the detuning between certain energy levels of interest [53–61]. This approach allows for an entangling gate to be created between: a qubit and numerous resonator modes [56], a qubit and a single resonator [57,58], two tunable transmons coupled to a mediating resonator [50,57], or two transmon qubits coupled via an adjustable mediating qubit [50,57]. Overall, this alternative approach offers potential benefits in terms of flexibility and scalability for constructing a scalable quantum computer with Superconducting qubits.

This paper is divided into two parts, Part I proposes a scheme for realizing two-qubit quantum gates based on the experimental scheme presented in [62], particularly an entangling gate known as Dagwood Bumstead (DB) gate [63], using the system combining two capacitively coupled Josephson Superconducting qubits. While Part II exploring the performance of the DB gate using a state-of-the-art Superconducting quantum architecture. We also give a full quantum characterization of the two-qubit gate by running two different tomography experiments: quantum process tomography (QPT) and quantum state tomography (QST) on a real IBM's superconducting quantum computer. The rest of this paper is structured as follows: In Section "Setup and implementation", the system combining two Josephson phase qubits coupled to capacitance can be employed to implement different two-qubit quantum gates, specially the 2-qubit entangling gate DB. In Section "The actual implementation of the DB gate", we present the implementation of the two-qubit DB gate using an IBM quantum computer. In Section "QST experiments" and Section "QPT experiments", we construct QST and QPT experiments for the DB gate, respectively, to give a full characterization and verification of quantum states. We run these quantum experiments in three distinct environments (noisy, noiseless, and on a real quantum machine). Then results from running quantum experiments are used to reconstruct the density matrices as well as the process matrices. Measurement errors and fidelities are also compared, with a discussion in the same sections. Finally, we draw our conclusion in Section "Conclusion".

Part 1: A proposed scheme for implementing the two-qubit entangling gates

Setup and implementations

According to the electrical circuit experimentally designed, fabricated and carried out in [62], the system combining two Josephson phase qubits coupled to capacitance was successfully employed to implement and characterize an entangling universal two-qubit gate, SQiSW (the square root of i-SWAP) gate. The most straightforward way to couple two superconducting Josephson phase qubits is through an interdigitated capacitor, as depicted in Fig. 1. Each qubit retains its own set of wires, allowing the adjustment of individual parameters and the option to measure, read out, and operate on them separately or together [64,65]. Capacitive coupling enables coupling of qubits at microwave frequencies while providing effective isolation at lower frequencies, preventing flux bias signals on one qubit from affecting the other [24,66].

In this setup, a single-shot measurement is performed to obtain the state of each qubit simultaneously, as each Josephson phase qubit has its own design parameters and bias. Also, it can be operated on, adjusted, measured and read out separately or simultaneously [64,65]. The interaction Hamiltonian of this system, in the rotating frame, takes the form [62]:

$$H_{\text{int}} = \frac{\hbar\,\zeta}{2}(\sigma_{X_A}\,\sigma_{X_B} + \sigma_{Y_A}\,\sigma_{Y_B}), \tag{1}$$

where $\sigma_{X_A}\,\sigma_{Y_A}$ are Pauli spin operators for qubit A. With $\hbar = h/2\pi$, h is the Plank's constant, $\zeta \approx (C_c/C + C_c)\,\omega_{ge}^{A,B}$ represents the coupling strength corresponding to the circuit design parameters, C_c is the coupling capacitance, C is the qubit capacitance We consider here the same system parameters as [62], namely: $C = 1$ pF, $C_c = 2$ fF and, $\omega_{ge}^{A,B}/2\pi \approx 5 - 6$ GHZ, so that $\zeta/2\pi \approx 11$ MHz. Nonetheless, the fixed coupling strength; the qubit-qubit interaction can be minimized by biasing the qubit off resonance such that $|(\omega_{ge}^{A} - \omega_{ge}^{B})| \gg \zeta$. As shown in Eq. (1), Pauli's operators offer a concise method of expressing the interaction Hamiltonian. However, they do not provide an immediate or intuitive visual understanding of the system. Thus, it is helpful to rephrase the interaction Hamiltonian in a way that demonstrates its impact on the two-qubit states. The effect of H_{int} on the two-qubit states, in the state space defined by $|g_A, e_B\rangle$ and $|e_A, g_B\rangle$, can be written as:

$$H_{int} = \frac{\hbar\,\zeta}{2}(|g_A, e_B\rangle\langle e_A, g_B| + |e_A, g_B\rangle\langle g_A, e_B|) \tag{2}$$

where $|g_A, e_B\rangle = |g\rangle_A \otimes |e\rangle_B$, $|e\rangle_j$ and $|g\rangle_j$ are excited and ground states for qubit $j = A, B$ respectively. When we express H_{int} in this manner, we can observe that the coupling interaction exchanges the populations of the $|g_A, e_B\rangle$ and $\langle e_A, g_B|$ states. Since only these two states are interacting, we can represent the coupled qubit system using a reduced state space consisting solely of the $|g_A, e_B\rangle$ and $\langle e_A, g_B|$ states.

When the two qubits are biased on-resonance, ($\omega_{ge}^{A} \approx \omega_{ge}^{B}$), the interaction Hamiltonian coupling the two-qubit states, in the sense that the states amplitudes oscillate in accordance with the time evolution

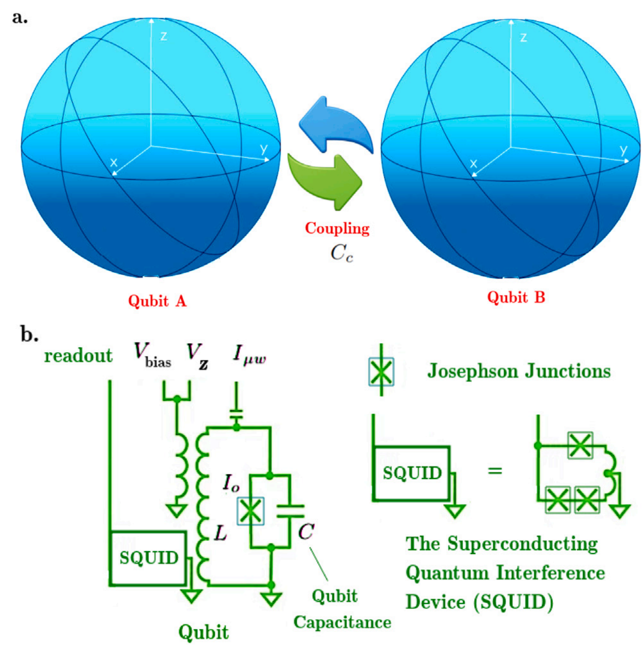

Fig. 1. Schematic circuit of the model a. Schematic diagram of two superconducting phase qubits that are capacitively coupled. **b.** Electrical schematic circuit of the Josephson superconducting qubit. Each qubit junction, marked by a single cross, has a critical current I_0 and is connected to an external capacitor C and inductor L. The qubits are coupled through an interdigitated capacitor $C_c = 2$ fF, which creates an interaction of $g/2 = 11$ MHz. The qubit is biased with V_{bias}, microwave control is applied using $I_{\mu w}$, and qubit readout is done using a three Josephson-junctions superconducting quantum interference device (SQUID) marked by three crosses and read out. The qubits can be biased on and off resonance using fast pulses on the V_Z lines.

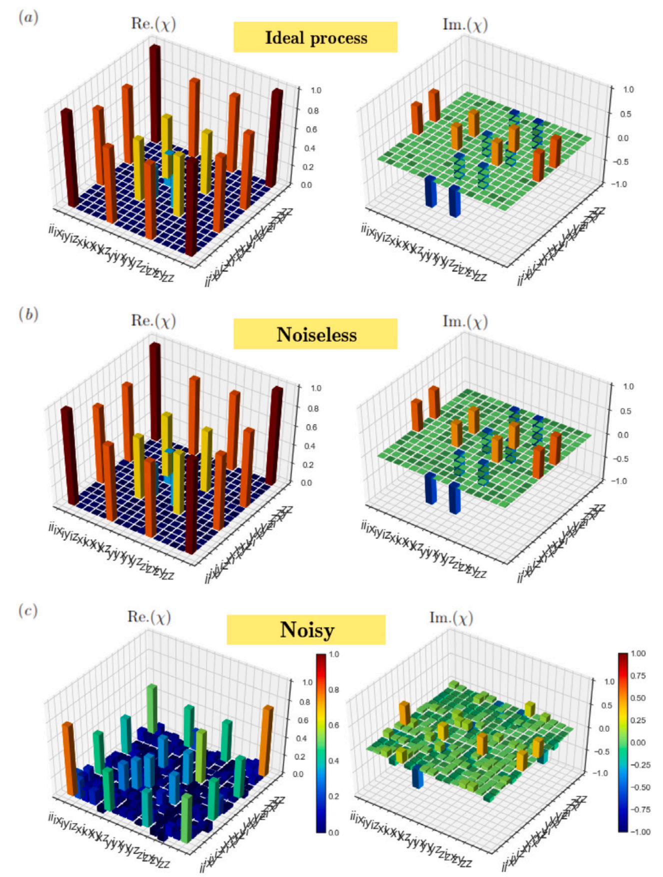

Fig. 2. Two-qubit QPT of the $\hat{\mho}_{2\pi/5}$ gate executed in different environments: (a) Real ($Re.(\chi)$) and imaginary ($Im.(\chi)$) parts of the ideal process matrix for the two-qubit gate $\hat{\mho}_{2\pi/5}$, which does not hold effects arising from decoherence, (perfect $\hat{\mho}_{2\pi/5}$ gate in the Pauli basis) $II, IX, IY, IZ, XI, XX, XY, XZ, YI, YX, YY, YZ, ZI, ZX, ZY$ and ZZ. (b) Real and imaginary parts of the process matrix from running QPT experiments in a noise-free environment. (c) Real and imaginary parts of the process matrix from running QPT experiments in a noisy environment.

operator $\mho_{\text{int}}$ as shown in Eq. (3). In the RWA [67], this unitary two-qubit transformation takes the form

$$\begin{aligned}\hat{\mho}_{\zeta t_g} =& \cos(\zeta t_g/2)\big(|g_A,g_B\rangle\langle e_A,e_B| + |e_A,e_B\rangle\langle g_A,g_B|\big)\\ &- i\sin\big(\zeta t_g/2)(|e_A,g_B\rangle\langle g_A,e_B| + |g_A,e_B\rangle\langle e_A,g_B|\big)\\ &+ |g_A,g_B\rangle\langle g_A,g_B| + |e_A,e_B\rangle\langle e_A,e_B|,\end{aligned} \tag{3}$$

where t_g is the interaction time, one way to express the concept of "H_{int}" is to use a rotation around the x-axis at an angle of ϖ, where "ϖ" refers to the duration that qubits are on resonance. When considering a single qubit, this rotation can be written as the quantum operation $X_\varpi = \begin{pmatrix}\cos(\varpi/2) & -i\sin(\varpi/2)\\ -i\sin(\varpi/2) & \cos(\varpi/2)\end{pmatrix}$. Thus, the unitary two-qubit matrix, $\hat{\mho}_{\zeta t_g}$, can be used to represent H_{int}, which describes a rotation (X_ϖ) between the $|g_A, e_B\rangle$ and $|e_A, g_B\rangle$ states in the two-qubit basis set $\{|g\rangle_A\otimes|g\rangle_B,\ |g\rangle_A\otimes|e\rangle_B,\ |e\rangle_A\otimes|g\rangle_B,\ |e\rangle_A\otimes|e\rangle_B\}$. The matrix operator corresponding to this unitary can be written as follows:

$$\hat{\mho}_{\zeta t_g} = \begin{pmatrix}1 & 0 & 0 & 0\\ 0 & \cos(\zeta t_g/2) & -i\sin(\zeta t_g/2) & 0\\ 0 & -i\sin(\zeta t_g/2) & \cos(\zeta t_g/2) & 0\\ 0 & 0 & 0 & 1\end{pmatrix} \tag{4}$$

In this system, it was demonstrated that high fidelity single-qubit operations can be used to prepare the 2-qubit basis states with state fidelity of 98% [62]. For an interaction time $\zeta t_g = \pi$, the iSWAP gate is formed [62]. The gate swapped the state amplitudes such that $|g\rangle\otimes|e\rangle \rightarrow -i|e\rangle\otimes|g\rangle, |e\rangle\otimes|g\rangle \rightarrow -i|g\rangle\otimes|e\rangle$. Whereas, by coupling for one-half this time, $\zeta t_g = \pi/2$, the two-qubit universal entangling gate SQiSW [62] is realized. The gate transforms the basis states such that $|g\rangle_A\otimes|e\rangle_B \rightarrow \frac{1}{\sqrt{2}}|g\rangle_A\otimes|e\rangle_B - \frac{i}{\sqrt{2}}|e\rangle_A\otimes|g\rangle_B$ and $|e\rangle_A\otimes|g\rangle_B \rightarrow \frac{-i}{\sqrt{2}}|g\rangle_A\otimes|e\rangle_B + \frac{1}{\sqrt{2}}|e\rangle_A\otimes|g\rangle_B$.

When coupling for $\zeta t_g = 2\pi/5$, the dynamical evolution in Eq. (3) progresses to realize a novel two-qubit gate. The unitary operator corresponding to this gate reads,

$$\hat{\mho}_{2\pi/5} = \begin{pmatrix}1 & 0 & 0 & 0\\ 0 & \frac{1}{4}(1+\sqrt{5}) & -\frac{i}{2\sqrt{2}}\sqrt{5-\sqrt{5}} & 0\\ 0 & -\frac{i}{2\sqrt{2}}\sqrt{5-\sqrt{5}} & \frac{1}{4}(1+\sqrt{5}) & 0\\ 0 & 0 & 0 & 1\end{pmatrix} \tag{5}$$

This gate transforms the basis states such that:

$$|g\rangle_A\otimes|g\rangle_B \rightarrow |g\rangle_A\otimes|g\rangle_B,$$

$$|g\rangle_A\otimes|e\rangle_B \rightarrow \frac{1}{4}(1+\sqrt{5})\,|g\rangle_A\otimes|e\rangle_B - \frac{i}{2\sqrt{2}}\sqrt{5-\sqrt{5}}\,|e\rangle_A\otimes|g\rangle_B,$$

$$|e\rangle_A\otimes|g\rangle_B \rightarrow \frac{-i}{2\sqrt{2}}\sqrt{5-\sqrt{5}}\,|g\rangle_A\otimes|e\rangle_B + \frac{1}{4}(1+\sqrt{5})\,|e\rangle_A\otimes|g\rangle_B,$$

$$|e\rangle_A\otimes|e\rangle_B \rightarrow |e\rangle_A\otimes|e\rangle_B.$$

While the CNOT gate [32,68–71] has gotten the greatest prominence in quantum computation, this qubit architecture allows for another -simpler- entangling gate, the DB gate [63]. This gate appears directly from the time evolution of the Hamiltonian for two coupled flux-biased phase qubits [70]. Compared to the CNOT gate, the DB gate has a shorter pulse sequence, which is important for performing as many gate operations as feasible before coherence is lost. The DB gate can be realized by letting two coupled qubits evolve under the interaction Hamiltonian Eq. (1) for three-fourths the time required for

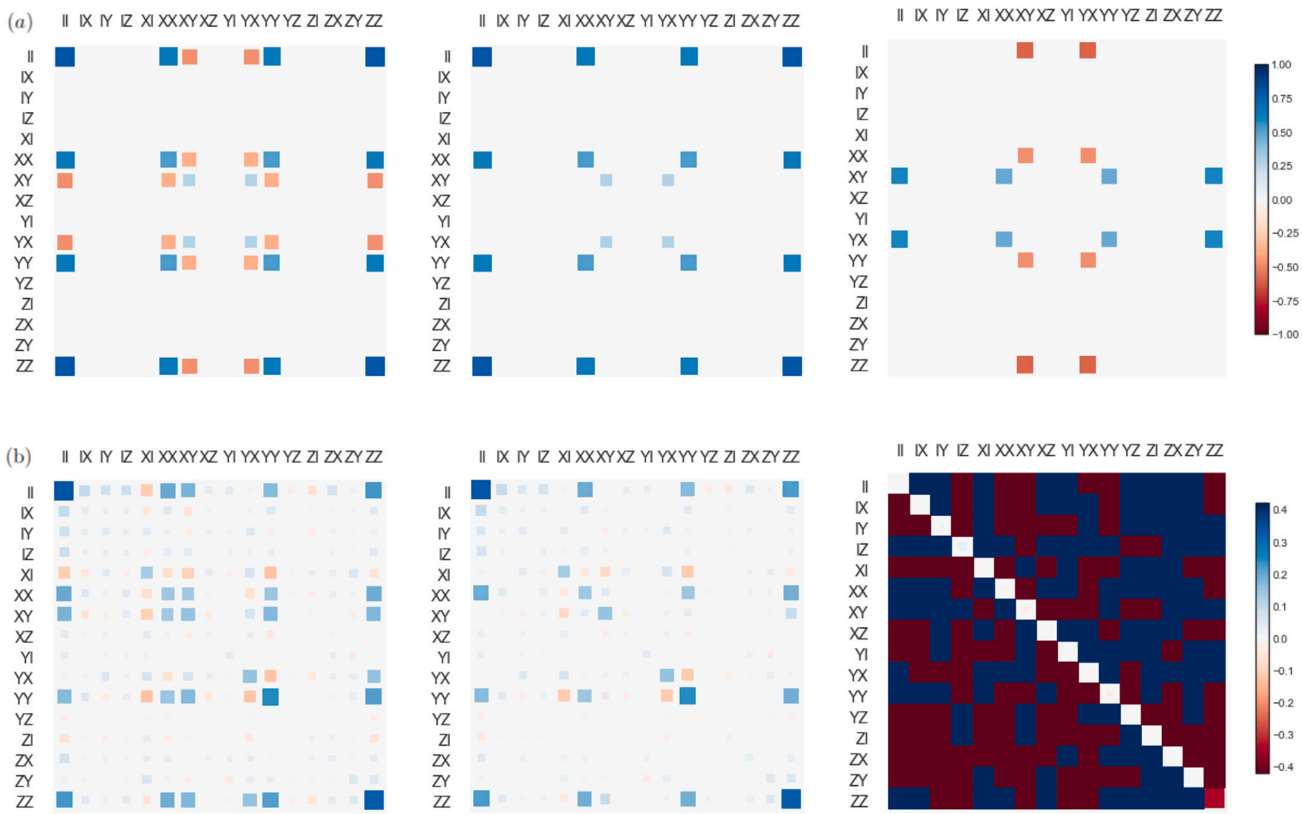

Fig. 3. Quantum process tomography of the two-qubit gate $\hat{\mho}_{2\pi/5}$. (a) Visualizations of the ideal process matrix of the two-qubit QPT of $\hat{\mho}_{2\pi/5}$ gate, which does not hold effects arising from decoherence, on the sixteen two-qubit basis states in the Pauli basis: $II, IX, IY, IZ, XI, XX, XY, XZ, YI, YX, YY, YZ, ZI, ZX, ZY$, and ZZ, as Hinton diagrams. (b) Two qubit process tomography of $\hat{\mho}_{2\pi/5}$ gate in a noisy environment using the IBM's 27-qubit noisy simulator, which includes effects caused by decoherence from previous quantum experiments. *The left panel* depict the combined parts, while the middle and right plots show the real and imaginary parts, respectively. We demonstrate an average gate fidelity of 0.85450, while the process fidelities were 0.9837423 and 0.39840 in noiseless and noisy environment, respectively.

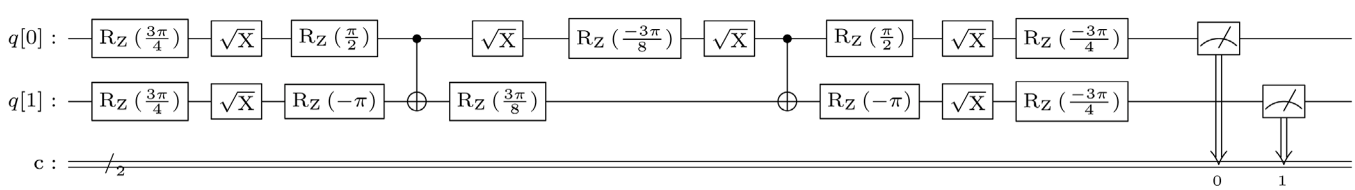

Fig. 4. A schematic circuit decomposition that is equivalent to the DB two-qubit entangling gate. The gate is broken down into a set of single-qubit gates including the rotation gates R_Z and the square root of NOT gate ($\sqrt{X}$) with only two controlled-NOT (CNOT) gates.

the iSWAP operation, $\zeta t_g = 3\pi/4$. The resulting matrix for the coupling interaction reduces to

$$\hat{\mho}_{DB} = \hat{\mho}_{3\pi/4} = \begin{pmatrix} 1 & 0 & 0 & 0 \\ 0 & \frac{1}{2}\sqrt{2-\sqrt{2}} & -\frac{i}{2}\sqrt{2+\sqrt{2}} & 0 \\ 0 & -\frac{i}{2}\sqrt{2+\sqrt{2}} & \frac{1}{2}\sqrt{2-\sqrt{2}} & 0 \\ 0 & 0 & 0 & 1 \end{pmatrix} \qquad (6)$$

An equivalent quantum circuit representation for the DB gate is shown in Fig. 4. The gate transforms the basis states as follows:

$$|g\rangle_A \otimes |g\rangle_B \rightarrow |g\rangle_A \otimes |g\rangle_B,$$

$$|g\rangle_A \otimes |e\rangle_B \rightarrow \frac{1}{2}\sqrt{2-\sqrt{2}}\,|g\rangle_A \otimes |e\rangle_B - \frac{i}{2}\sqrt{2+\sqrt{2}}\,|e\rangle_A \otimes |g\rangle_B,$$

$$|e\rangle_A \otimes |g\rangle_B \rightarrow \frac{-i}{2}\sqrt{2+\sqrt{2}}\,|g\rangle_A \otimes |e\rangle_B + \frac{1}{2}\sqrt{2-\sqrt{2}}\,|e\rangle_A \otimes |g\rangle_B,$$

$$|e\rangle_A \otimes |e\rangle_B \rightarrow |e\rangle_A \otimes |e\rangle_B.$$

The DB-gate has an entangling power [72] of 1.96/9. It is of special significance as itself belongs to the canonical family, it is natively available to systems where iSWAP gate is available, and it can arise naturally in such systems [63,73].

To gain insights into the gate's performance and how it affects different qubit states, a quantum process tomography (QPT) analysis for the $\hat{\mho}_{2\pi/5}$ gate was performed. QPT is a vital technique in the field of quantum computing, as it enables the validation of quantum gates and the identification of flaws in configuration and gate design. The objective of QPT is to obtain a precise description of the quantum process or dynamical map through a series of carefully designed experiments.

In our analysis, we utilized the Choi–Jamiolkowski representation, also known as the Choi matrix [77,78], to fully characterize our quantum operations. Specifically, we designed and perform QPT analysis for the 2-qubit gates, and based on the results, we re-constructed the Choi matrices χ for these gates. To quantitatively compare the reconstructed (estimated) Choi matrix with theoretical (ideal) expectations, we calculated the process fidelity [76] of noisy quantum channels. This fidelity value represents how closely the measured Choi matrices match the ideal process, with a value of 1 indicating a perfect match. Further discussions of both QPT and QST are given in Section "Quantum tomography study of DB gate on an IBM's quantum computer". Detailed descriptions of QPT theory are available in [79–83].

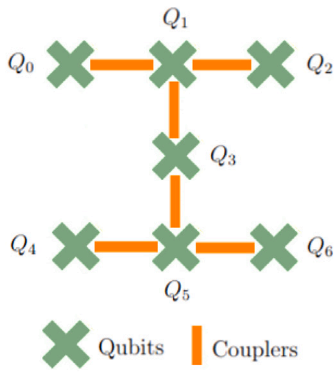

Fig. 5. A schematic of the *ibm_oslo* quantum machine from the IBM Quantum Experience. Seven superconducting transmon qubits construct the processor, which runs at a very low temperature, close to absolute zero Kelvin. The processor has a median qubit frequency of 5.046 GHz, and can outperform up to one hundred quantum circuits, with 20,000 maximum shots.

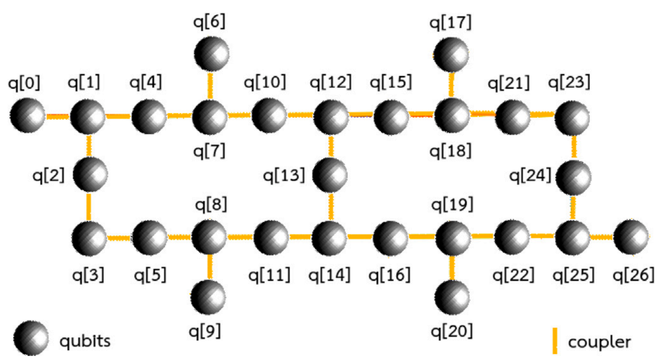

Fig. 6. The schematic diagram of IBM's 27-qubit noisy simulator, which includes effects caused by decoherence from previous quantum experiments. The noise backends are designed to mimic the behavior of actual IBM Quantum systems.

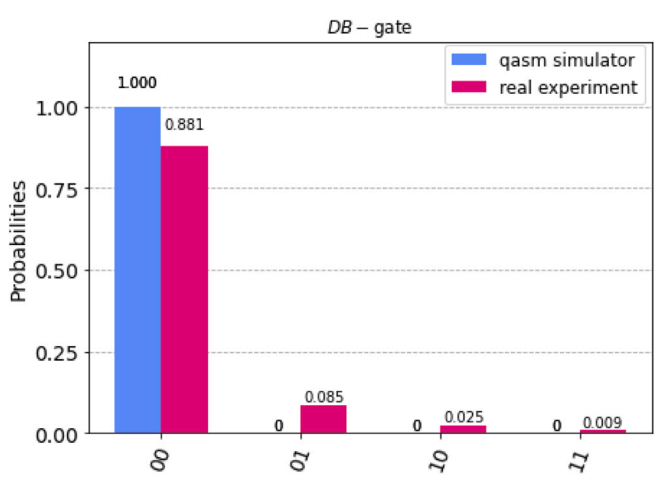

Fig. 7. Measurement outcomes from the two-qubit DB gate's actual implementation. Result obtained after conducting the experiment for 4096 shots on both a *qasm_simulator* and a real quantum computer, *ibm_oslo*. Small probabilities result from noisy in the quantum computation.

Two-qubit QPT for the $\hat{\mho}_{2\pi/5}$ gate is presented in Fig. 2. Where Fig. 2(a) presents, real ($Re.(\chi)$) and imaginary ($Im.(\chi)$) parts of the ideal process matrix (theoretically expected) for the perfect $\hat{\mho}_{2\pi/5}$ gate in the Pauli basis, which does not include decoherence effects; Fig. 2(b) illustrates real and imaginary parts of the process matrix from running QPT experiments in a noise-free environment. Fig. 2(c) Real and imaginary parts of the process matrix from running QPT experiments in a noisy environment. The process matrices for the $\hat{\mho}_{2\pi/5}$ gate can be further analyzed by separating it into its combined, real, and imaginary parts, and plotted as a Hinton diagram as shown in Fig. 3. The combined parts are depicted in the left-panel, while the real (imaginary) parts are shown in the middle (right) plots, respectively. By analyzing these visualizations, one can gain insights into the gate's performance and how it affects different qubit states. We demonstrate an average gate fidelity of 0.85450. In using QPT to estimate the gate fidelity [74,75], we demonstrate process fidelities of 0.9837423 and 0.39840 in noiseless and noisy environment, respectively.

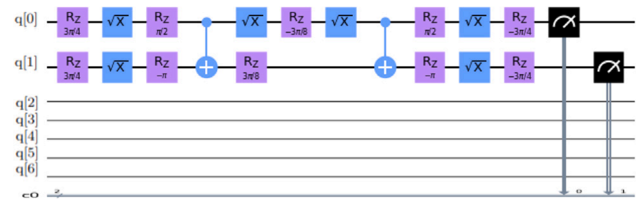

Fig. 8. Equivalent quantum circuit for the DB two-qubit entangling gate. The gate is deconstructed in terms of single-qubit gates with only two CNOTs. This quantum circuit is executed for 4096 shots, on the IBM quantum machine, *ibm_oslo*.

Table 1
The average gate fidelities and the process fidelities of the two-qubit quantum gates: SQiSW, $\hat{\mho}_{2\pi/5}$ and DB, calculated in different settings.

Two-qubit gate	Fidelity	
	$\mathcal{F}_{av}$ [a]	$\mathcal{F}_p$ [b] (noisy)
SQiSW [62]	0.78284	0.61 [62]
$\hat{\mho}_{2\pi/5}$ (Eq. (5))	0.85451	0.39840
DB (Eq. (6))	0.58236	0.88213

[a] Average gate fidelity [74,75].
[b] Process fidelity [76] from running QPT in noisy environment.

Table 1 illustrates the average gate and the process fidelities of the two-qubit gates SQiSW, $\hat{\mho}_{2\pi/5}$ and DB. In a noisy environment, the DB gate has the highest process fidelity F_p(noisy), followed by the SQiSW gate and then $\hat{\mho}_{2\pi/5}$ gate. In what follows, our focus is to present a thorough characterization of the two-qubit entangling gate (DB), with the goal of investigating the challenges posed by errors in this gate on NISQ devices.

Part 2: Exploring the Performance of DB Gate on an IBM's Quantum Computer

The actual implementation of the DB gate

In this work, to outperform our implementations, we used the IBM Quantum Experience [3] real machine, known as *ibm_oslo*. This processor is made up of seven superconducting transmon qubits, which are arranged as shown in Fig. 5.

The Basis gates of this architecture are: the identity (I), the NOT gate (X), the square root of NOT gate ($\sqrt{X}$), the rotation gate around z-axis (RZ), and the Controlled-NOT gate (CNOT). The coupling map between qubits is CNOT: $q[0]-q[1]$, CNOT: $q[1]-q[2]$, CNOT: $q[1]-q[3]$, CNOT: $q[1]-q[0]$, CNOT: $q[2]-q[1]$, CNOT: $q[3]-q[1]$, CNOT: $q[3]-q[5]$, CNOT: $q[4]-q[5]$, CNOT: $q[5]-q[4]$, CNOT: $q[5]-q[3]$, CNOT: $q[5]-q[6]$, and CNOT: $q[6]-q[5]$.

The median qubit frequency ($\omega/2\pi$) of this processor [3] is 5.046 GHz, the median relaxation times $T1$ and $T2$ are 10.962 μs and 39.84 μs, respectively. [84]. The median qubit anharmonicity ($\gamma/2\pi$) is −0.34293 GHz, the qubit readout assignment error ($\xi(R)$) has a median of 1.17×10^{-2}. The qubit flip probabilities from $|1\rangle$ to $|0\rangle$ (ζ) and from $|0\rangle$ to $|1\rangle$ (η), have a median of 1.24×10^{-2} and 1.2×10^{-2}, respectively. The readout length (δ) is 910.2222 ns, Pauli error rates

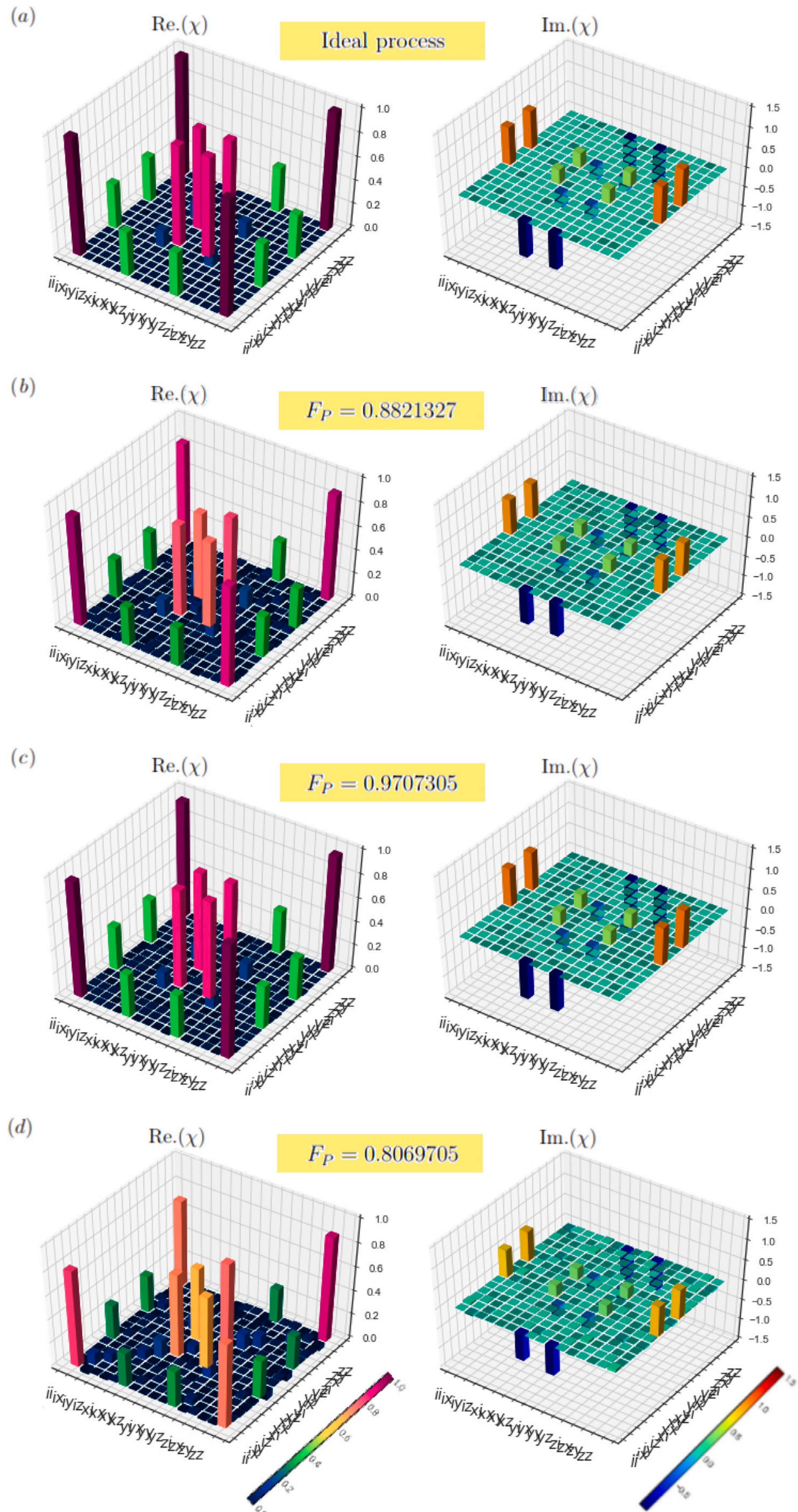

Fig. 9. Real and imaginary parts of the Choi matrices, reconstructed from 144 quantum circuits that executed in the QPT experiments for the two-qubit DB gate, with the final results for the 576 measurement outcomes across all circuits. (a) The perfect Choi matrix (theoretical expectations). (b) QPT experiments carried out in a noisy environment. (c) QPT experiments were carried out in a noise-free environment. (d) QPT experiments performed on a real IBM quantum computer. The QPT experiments were repeated for 4,000 times in each setting, we obtain a process fidelity of 0.8821327, 0.9707305 and 0.8069705, respectively. The running time in the *ibm_oslo* machine was 2 m and 43.5 s.

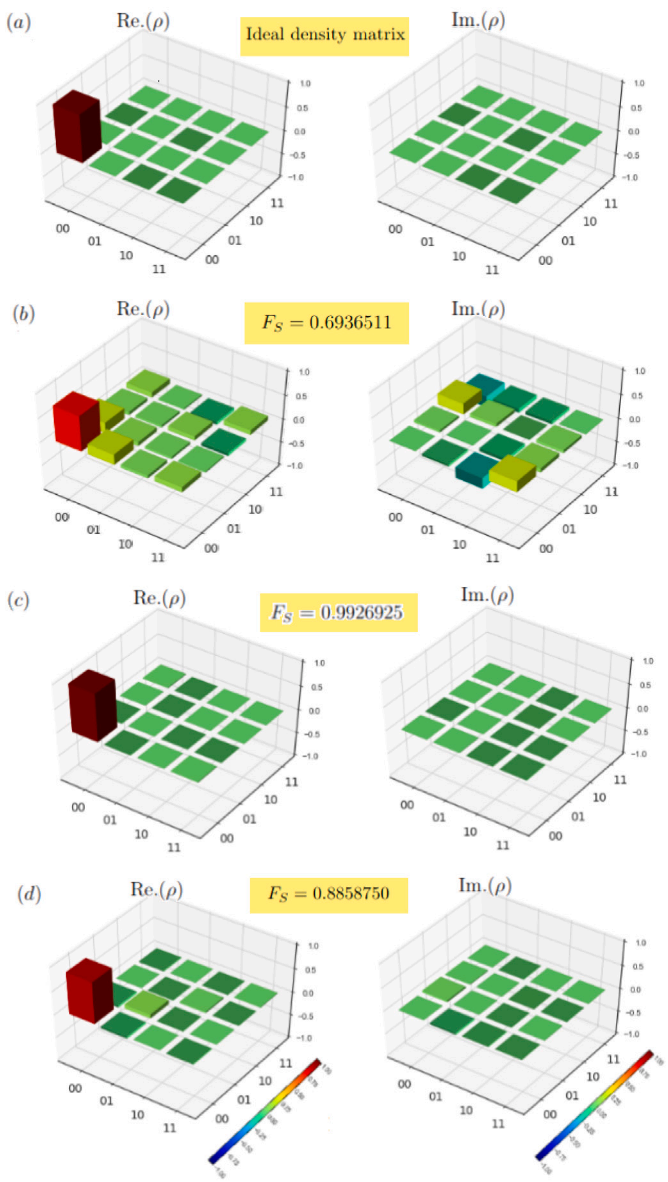

Fig. 10. Real and (imaginary) parts Re.(ρ) (Im.(ρ)) of the density matrices, rebuilt from QST experiments of the two-qubit DB gate. (a) The perfect density matrix (theoretical expectations). (b) QST experiments carried out in a noisy environment. (c) QST experiments were carried out in a noise-free environment. (d) QST experiments performed on a real IBM quantum computer. The QST experiments are repeated for 4000 times in each setting, we obtain a state fidelity of 0.69365, 0.99269 and 0.88587, respectively. The running time in the *ibm_oslo* machine was 13.8 s.

Table 2
The general performance of the seven qubits Superconducting quantum computer, *ibm_oslo*. With Qubit frequency ($\omega/2\pi$), anharmonicity ($\gamma/2\pi$), readout length (δ), readout assignment error (ξ), the bit flip probabilities (ζ and η), and the relaxation times $T1$ and $T2$, accessed on September 11, 2022.

q[i]	$T1$ (μs)	$T2$ (μs)	$\omega/2\pi$ (GHz)	$\gamma/2\pi$ (GHz)	$\xi(R)$	ζ (%)	η (%)	δ (ns)
q[0]	165.51	110.68	4.925	−0.34448	0.0098	0.0124	0.0072	910.222
q[1]	137.93	39.840	5.046	−0.34293	0.0117	0.0140	0.0094	910.222
q[2]	152.04	28.470	4.962	−0.34565	0.0071	0.0084	0.0058	910.222
q[3]	98.280	38.530	5.108	−0.34186	0.0171	0.0124	0.0218	910.222
q[4]	174.68	191.83	5.011	−0.34389	0.0220	0.0210	0.0230	910.222
q[5]	126.02	34.840	5.173	−0.34234	0.0116	0.0112	0.0120	910.222
q[6]	105.89	246.23	5.319	−0.33883	0.0287	0.0314	0.0260	910.222

have a median of 2.166×10^{-4} while, the median CNOT gates Error (CNOTe) is 6.3405×10^{-3}, with a median gate time 286.222 ns.

Table 3
Error rates of the 1-qubit Pauli X gate and controlled-NOT gates (CNOTe) between different qubits $q[i]$ with the corresponding gate time during operating on the *ibm_oslo* quantum computer, as accessed on September 11, 2022.

$q[i]$	Pauli's$_e$ [a]	Coupling map	Gate time (ns)	CNOTe [b]
$q[0]$	0.0002978	CNOT: $q[0]-q[1]$	341.333	0.007126
$q[1]$	0.0001952	CNOT: $q[1]-q[2]$	248.889	0.005801
		CNOT: $q[1]-q[3]$	263.111	0.007571
		CNOT: $q[1]-q[0]$	412.444	0.007126
$q[2]$	0.0002166	CNOT: $q[2]-q[1]$	213.333	0.005801
$q[3]$	0.0004017	CNOT: $q[3]-q[1]$	334.222	0.007571
		CNOT: $q[3]-q[5]$	238.222	0.005110
$q[4]$	0.0001985	CNOT: $q[4]-q[5]$	305.333	0.009309
$q[5]$	0.0003516	CNOT: $q[5]-q[4]$	341.333	0.009309
		CNOT: $q[5]-q[3]$	167.111	0.005110
		CNOT: $q[5]-q[6]$	405.333	0.007232
$q[6]$	0.0002141	CNOT: $q[6]-q[5]$	334.222	0.007232

[a] Error rates of the controlled-NOT gates between different qubits $q[i]$.
[b] Pauli's error rates.

Detailed device specifications of the *ibm_oslo* and qubit parameters are presented in Table 2. The coupling map between qubits with the corresponding CNOT gate time are shown in Table 3. Single-qubits Pauli as well as error rates of the CNOT gates' between qubits are displayed in Table 3.

Here, the two-qubit DB gate is decomposed into the main gate set of IBM's quantum architecture, in terms of a set of single-qubit gates and only two controlled-NOT gates, as shown in Fig. 8. Then, the quantum circuit was executed for 4,096 shots, on both the *qasm_simulator* and the *ibm_oslo* quantum processor (see Table 4).

The *qasm_simulator* predicts that for 4096 shots, the classical register returns $|11\rangle$ for 4,096 of the time, and gives zero for the computational basis $|01\rangle$, $|10\rangle$ and $|11\rangle$. Whereas in the real experiment on the *ibm_oslo*, measurement outcomes return: $|11\rangle$ for 3,609 of the time, $|10\rangle$ for 348 of the time, $|01\rangle$ for 102 of the time, and $|11\rangle$ for 37 of the time. Measurement outcomes from the actual implementation of the two-qubit gate on both a *qasm_simulator* and a quantum computer are shown in Fig. 7. The median qubit frequency ($\omega/2\pi$) is 5.04644 GHz, the median relaxation times $T1$ and $T2$ are respectively 139.6641 μs and 39.87324 μs. The median qubit anharmonicity ($\gamma/2\pi$) is −0.3429 GHz, whereas, the qubit readout assignment error ($\xi(R)$) has a median of 0.014199. The qubit flip probabilities from $|1\rangle$ to $|0\rangle$ (ζ) and from $|0\rangle$ to $|1\rangle$ (η), have a median of 0.0138 and 0.014599, respectively. With a readout length (δ) of 910.2222 ns.

Quantum tomography study of DB gate on an IBM's quantum computer

QPT experiments

Quantum process tomography is a critical procedure for validating quantum gates and identifying flaws in configuration and gate design [85,86]. The goal of QPT is to find a description of the quantum process (dynamical map) from a series of quantum experiments. QPT necessitates initializing the qubits-system in a suitable density matrix basis, then applying a process to these basis states, and finally describing the output quantum states using a quantum state tomography algorithm. Detailed descriptions of the QPT theory are provided in [79–83]. Through our QPT experiments, we used the Choi–Jamiolkowski [77,78] representation (Choi matrix) to fully characterize our quantum operations.

In this section, we design and run QPT experiments for the DB gate [87]. These quantum experiments are carried out in three environments: a noisy environment, a noise-free environment, and a real IBM

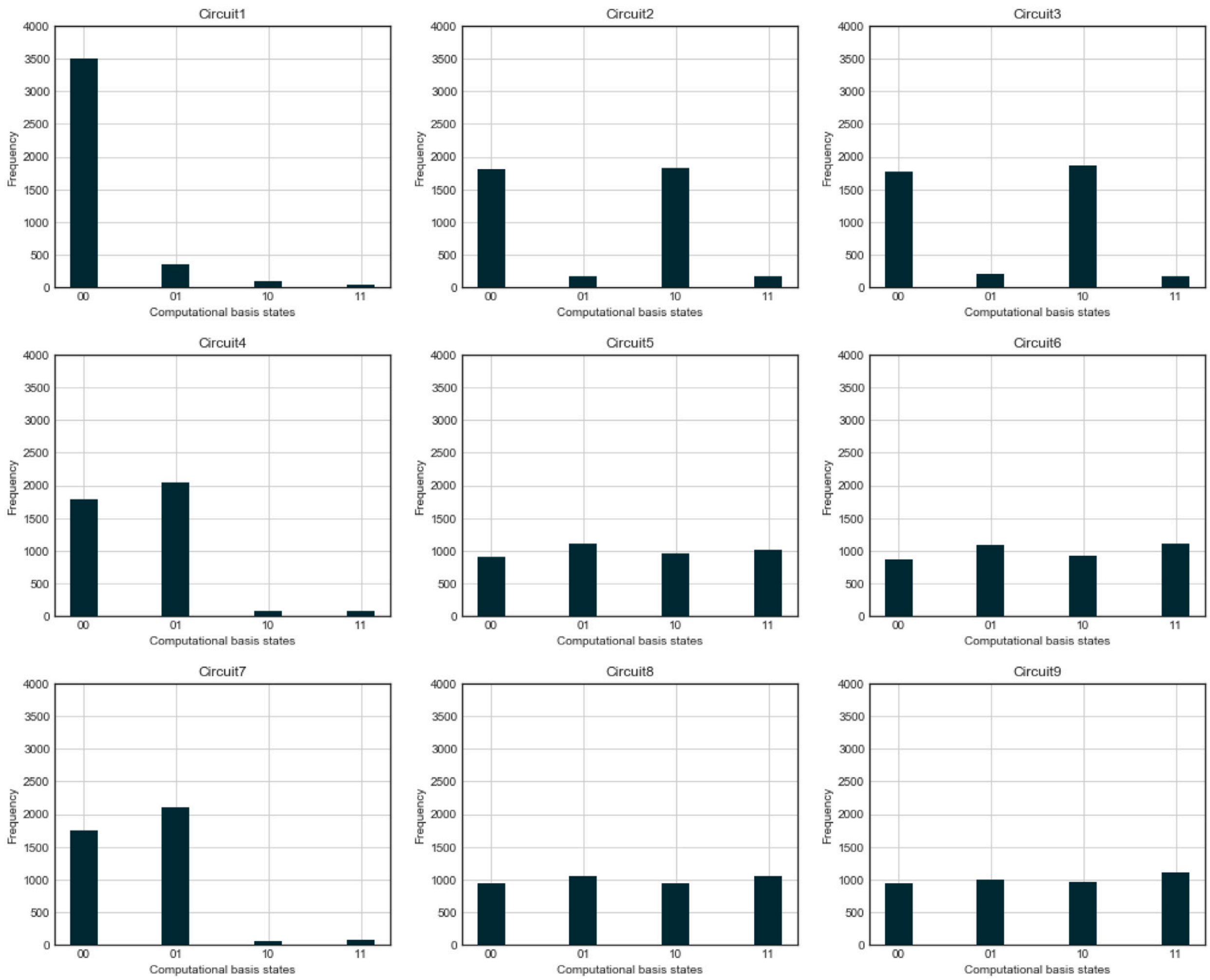

Fig. 11. Experimental results over all QST circuits. The results collected from a total of 9 measurement circuits that executed in the QST experiments for the two-qubit DB gate. With the final results for the 36 measurement outcomes over all circuits of all qubits in the Pauli bases $\{XX, XY, XZ, YX, YY, YZ, ZX, ZY, ZZ\}$. These quantum experiments are repeated for 4000 shots for each measurement basis on the real IBM's quantum computer, *ibm_oslo*. Running time in system was 13.8 s.

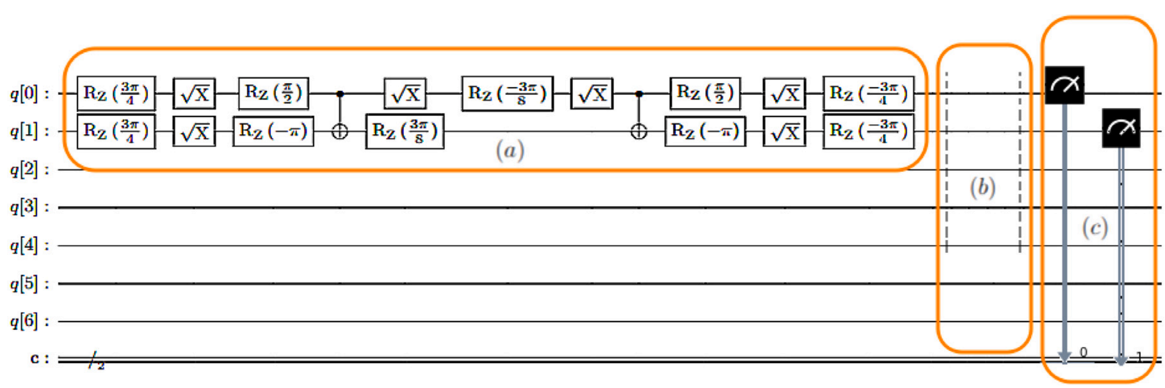

Fig. 12. QST design of the two-qubit DB gate. State preparation circuit (a) appended for the nine QST circuits,(b). Followed by measurements of all qubits in the Pauli bases $\{XX, XY, XZ, YX, YY, YZ, ZX, ZY, ZZ\}$, (c).

quantum computer. In each environment, the QPT experiments were repeated 4,000 times. We use the results to construct the Choi matrices for the DB gate. Calculating the process fidelity ($0 \leq \mathcal{F}_p \leq 1$) of noisy quantum channels [76] demonstrates quantitative comparison, which indicates how close the measured Choi matrices are to theoretical expectations (ideal process). Fig. 9 depicts the real and imaginary parts of the Choi matrices, as well as the process fidelities corresponding to the QPT experimental realizations in the three environments.

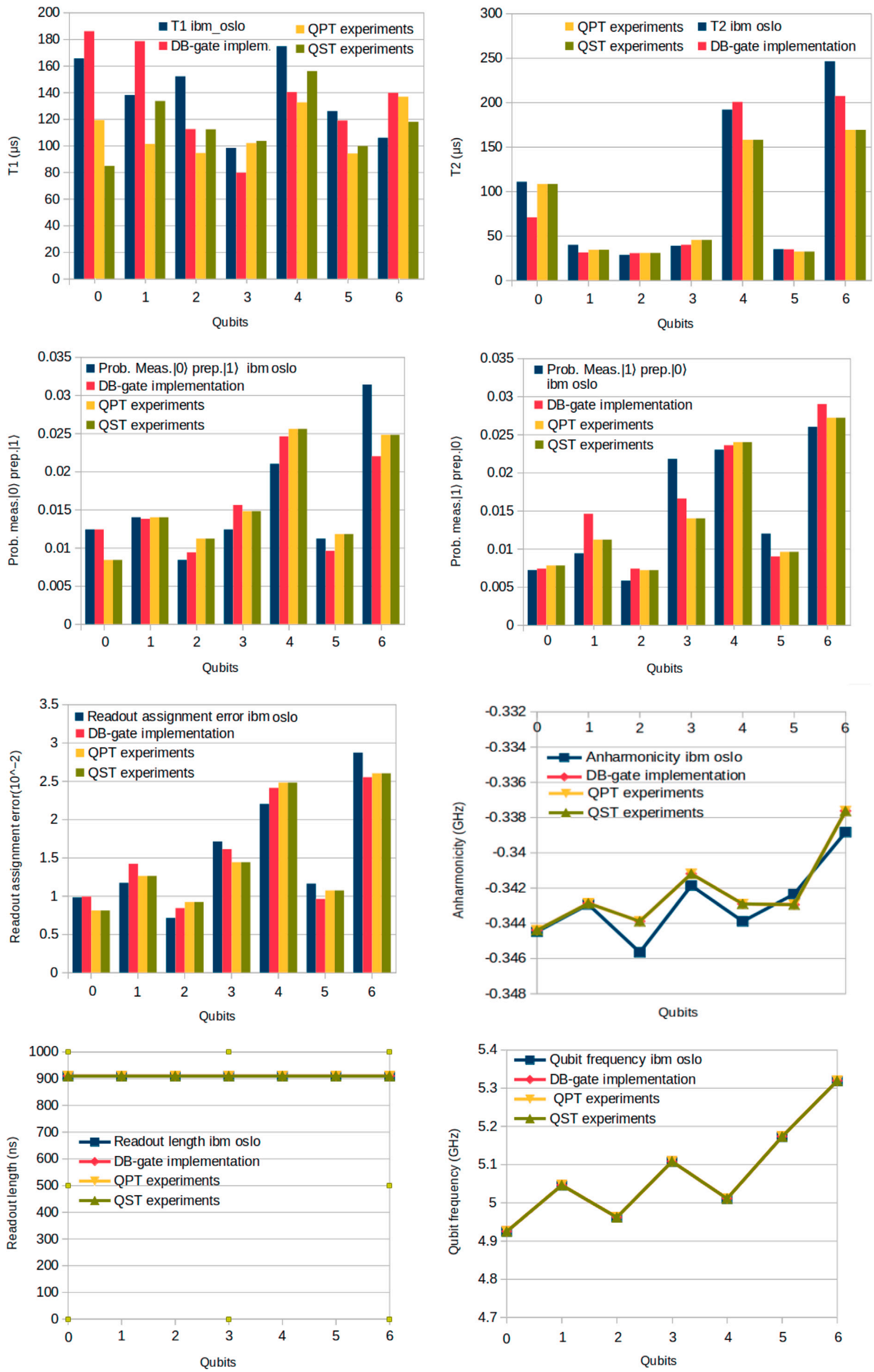

Fig. 13. Processor performance, parameters distribution and readout errors for each qubit across the *ibm_oslo* quantum computer, during the execution of both the QPT and the QST experiments.

Table 4
The experimental system characteristics during performing the experimental implementation of DB gate for 4,096 shots on the *ibm_oslo*. The running time on the system was 5.1 s.

$q[i]$	$T1$ (μs)	$T2$ (μs)	$\omega/2\pi$ (GHz)	$\gamma/2\pi$ (GHz)	$\xi(R)$	ζ (%)	η (%)	δ (ns)
$q[0]$	186.0054	70.66683	4.925055	−0.344396	0.009900	0.0124	0.007399	910.2222
$q[1]$	178.4910	31.15843	5.046440	−0.342862	0.014199	0.0138	0.014599	910.2222
$q[2]$	112.3796	30.41982	4.962016	−0.343890	0.008399	0.0094	0.007400	910.2222
$q[3]$	79.67078	39.87324	5.108289	−0.341193	0.016100	0.0156	0.016599	910.2222
$q[4]$	140.1864	200.5518	5.011118	−0.342900	0.024100	0.0246	0.023599	910.2222
$q[5]$	118.8671	34.66211	5.173375	−0.342940	0.009600	0.0096	0.009000	910.2222
$q[6]$	139.6641	207.2135	5.319373	−0.337626	0.025500	0.0220	0.029000	910.2222

Table 5
The experimental system parameters that used during running the QST experiments of the DB gate, by the IBM quantum computer, *ibm_oslo*.

$q[i]$	$T1$ (μs)	$T2$ (μs)	$\omega/2\pi$ (GHz)	$\gamma/2\pi$ (GHz)	$\xi(R)$	ζ (%)	η (%)	δ (ns)
$q[0]$	84.79215	108.2099	4.925052	−0.344395	0.008099	0.00840	0.007800	910.2222
$q[1]$	133.5468	34.16858	5.046449	−0.342862	0.012599	0.01400	0.011199	910.2222
$q[2]$	112.2141	30.62661	4.962017	−0.343890	0.009199	0.01120	0.007200	910.2222
$q[3]$	103.5158	45.19890	5.108277	−0.341193	0.014399	0.01480	0.014000	910.2222
$q[4]$	156.0072	157.7809	5.011111	−0.342900	0.024799	0.02559	0.024000	910.2222
$q[5]$	99.70150	32.20664	5.173382	−0.342940	0.010700	0.01180	0.009600	910.2222
$q[6]$	117.9182	168.9771	5.319378	−0.337626	0.026000	0.02480	0.027200	910.2222

We demonstrate a process fidelity of 0.8821327, 0.9707305 and 0.8069705 respectively corresponding to the QPT experiments for the DB gate via; a noisy simulation, noise-free environment, and on the IBM real machine *ibm_oslo*, as illustrated in Table 7.

Results obtained by repeating the quantum experiment for 4000 shots for each measurement basis on the *ibm_oslo*, over all the 144 QPT circuits, that were executed in the QPT experiments for the two-qubit DB gate, together with the final results for the 576 measurement outcomes over all circuits are used to rebuild the Choi matrices, which are presented in Figs. 9. Detailed device specifications of the *ibm_oslo* and qubit parameters that used during performing the QPT experiments are presented in Table 6. The median qubit frequency ($\omega/2\pi$) is 5.046449 GHz, the median relaxation times $T1$ and $T2$ are respectively 101.948 μs and 45.1989 μs. The median qubit anharmonicity ($\gamma/2\pi$) is −0.3429 GHz, whereas, the qubit readout assignment error ($\xi(R)$) has a median of 1.2599×10^{-2}. The qubit flip probabilities from $|1\rangle$ to $|0\rangle$ (ζ) and from $|0\rangle$ to $|1\rangle$ (η), have a median of 1.4×10^{-2} and 1.1199×10^{-2}, respectively. With a readout length (δ) of 910.2222 ns. Fig. 13 shows parameters distribution and readout errors for each qubit across the *ibm_oslo* quantum computer, as well as the processor performance while executing the QPT experiments.

QST experiments

A procedure for extracting a description of a system's quantum state from a sequence of quantum experiments is known as quantum state tomography. The approach for QST is to perform a series of repeated measurements, aiming to reconstruct or approximate the density matrix ρ that describes the state of an open quantum system. In doing so, a state preparation circuit must be appended to a series of measurements, with respect to different operators. The measurement data are then used to rebuild or approximate the state. A number of methods for reconstructing a valid description of the density matrix of the actual state obtained in the system from measured data have been proposed [88–92].

Here, we design and perform QST experiments for the two-qubit entangling gate. Quantum experiments are carried out in three environments: noisy, *qasm_simulator*, and on a real IBM quantum computer. The *qasm_simulator* was designed to simulate quantum circuits, both with and without noise. The *qasm_simulator* supports various simulation techniques, and each simulation technique has configurable settings, according to the circuits, and noise model. Although the *qasm_simulator* mimics a flawless (ideal) quantum computer, it can also be configured to mimic a real noisy quantum computer. The *qasm_simulator* was set up to simulate the perfect quantum computer while executing our experiments.

In contrast, noisy simulations were employed to compare with actual quantum systems. We used the 27-qubit IBM noisy simulator, as shown in Fig. 6, which includes effects caused by decoherence from past experimental implementations. The noise backends are built to mimic the behaviors of real IBM quantum architectures by utilizing noise models developed from system snapshots, collected from previous quantum experiments. Important information about the quantum system are stored in system snapshots, such as qubit properties, relaxation times (T1 and T2), coupling maps, and error rates. This data is useful for executing noisy simulations of the actual quantum systems. Readers are directed to [3,93] for more information on the *qasm_simulator*'s functionality as well as the IBM's backends.

In these experimental setups, we add measurements of all qubits in the X, Y, and Z Pauli bases, for the DB gate's appended state preparation circuit (shown in Fig. 12). As a result, nine measurement circuits must be executed for the two qubit DB gate. And the final result for all 36 measurement outcomes provides a tomographically overcomplete basis, allowing us to reconstruct the quantum state. This data is used to rebuild density matrices for DB gate, as shown in Fig. 10. This figure depicts the real- and imaginary- parts of the reconstructed density matrices obtained by running QST experiments for 4,000 shots on each measurement basis. Fig. 11 presents results from repeating the quantum experiment for 4,000 shots for each measurement basis on the *ibm_oslo*, with measurements across all the nine QST circuits that were executed during the tomography experiments for DB gate; and the final results for the 36 measurement outcomes across all circuits. The state fidelity for two input states (density matrices) is given by

$$\mathcal{F}_s(\rho_{\text{ideal}}, \rho_{exp.}) = \left(Tr\left[\sqrt{\sqrt{\rho_{\text{ideal}}}\,\rho_{exp.}\,\sqrt{\rho_{\text{ideal}}}} \right] \right)^2, \tag{7}$$

where ρ_{ideal} and $\rho_{exp.}$ are theoretical and experimental density matrices, respectively. The state fidelities $\mathcal{F}_S$ corresponding to the QST experiments for DB gate; with noiseless environment, noisy, and on the IBM real machine *ibm_oslo*, are 0.99269, 0.69365 and 0.88587 respectively, as summarized in Table 7. Table 5 displays the system experimental parameters used while running the QST experiment of the DB gate on IBM's quantum processor, *ibm_oslo*.

The median qubit frequency ($\omega/2\pi$) is 5.046449 GHz, the median relaxation times $T1$ and $T2$ are respectively 112.2141 μs and 45.1989 μs. The median qubit anharmonicity ($\gamma/2\pi$) is −0.3429 GHz, whereas, the qubit readout assignment error ($\xi(R)$) has a median of $1.2599{\times}10^{-2}$. The qubit flip probabilities from $|1\rangle$ to $|0\rangle$ (ζ) and from $|0\rangle$ to $|1\rangle$ (η), have a median of 1.4×10^{-2} and 1.1199×10^{-2}, respectively. With a readout length (δ) of 910.2222 ns.

Table 6
The experimental system parameters that used during running the QPT experiments (the 144 QPT circuits) of DB gate, by the IBM quantum computer, *ibm_oslo*.

$q[i]$	$T1$ (μs)	$T2$ (μs)	$\omega/2\pi$ (GHz)	$\gamma/2\pi$ (GHz)	$\xi(R)$	ζ (%)	η (%)	δ (ns)
$q[0]$	119.1475	108.2099	4.925052	−0.344395	0.008099	0.00840	0.007800	910.2222
$q[1]$	101.2761	34.16858	5.046449	−0.342862	0.012599	0.01400	0.011199	910.2222
$q[2]$	94.45657	30.62661	4.962017	−0.343890	0.009199	0.01120	0.007200	910.2222
$q[3]$	101.9480	45.19890	5.108277	−0.341193	0.014399	0.01480	0.014000	910.2222
$q[4]$	132.5345	157.7809	5.011111	−0.342900	0.024799	0.02559	0.024000	910.2222
$q[5]$	94.12509	32.20664	5.173382	−0.342940	0.010700	0.01180	0.009600	910.2222
$q[6]$	136.7163	168.9771	5.319378	−0.337626	0.026000	0.02480	0.027200	910.2222

Table 7
Comparable fidelities (the state $\mathcal{F}_S$, and the process $\mathcal{F}_p$ fidelities) demonstrated from running both QPT and QST experiments of the two-qubit entangling gate DB in different settings.

	Quantum process tomography			Quantum state tomography		
Gate Fidelity	$\mathcal{F}_p$ (noiseless)	$\mathcal{F}_p$ [a] (noisy)	$\mathcal{F}_p$ (IBM)	$\mathcal{F}_S$(noiseless)	$\mathcal{F}_S$ (noisy)	$\mathcal{F}_S$ (IBM)[b]
Value	0.97073	0.88213	0.80697	0.99269	0.69365	0.88587

[a] The process fidelity from running QPT experiments with noise.
[b] The state fidelity from running QPT experiments on the real quantum computer, *ibm_oslo*.

Fig. 13 shows the parameter distribution and readout errors for each qubit over the *ibm_oslo* quantum computer, in addition to the hardware performance while running the QST experiments. Comparable fidelities from running these quantum experiments in different settings (noise free, noisy and on a real quantum machine) are summarized in Table 7.

Conclusion

The presence of entangled states is essential to completely harness the power of quantum computation and quantum information processing. At the absence of such states, quantum computers cannot surpass the computational power of its classical counterparts. Although noisy intermediate-scale quantum computers (NISQ) have demonstrated superior performance in handling complex tasks compared to conventional computing schemes, the errors associated with two-qubit entangling gates are still a significant impediment to reaping the benefits of today's superconducting quantum computers.

In this paper, we presented a scheme to implement a natural two-qubit entangling gate, known as DB gate. Furthermore, we present and analyze an additional two-qubit quantum gate ($\hat{\mho}_{2\pi/5}$). The $\hat{\mho}_{2\pi/5}$ gate demonstrates an average gate fidelity of 0.85450. These implementations are based on the system joining two superconducting Josephson phase qubits coupled to capacitance. The DB gate is of particular importance, as it belongs to the canonical family, compared to the CNOT gate, the DB gate has a shorter pulse sequence, which is important for performing as many gate operations as possible before coherence is lost. Furthermore, we have investigated the challenges posed by errors in two-qubit entangling gate (DB) on NISQ devices, which have the potential to perform complex tasks more effectively than conventional computing schemes. We have analyzed an actual implementation of the two-qubit entangling DB gate, which can be implemented on a transmon-based superconducting qubit quantum computer.

To evaluate the performance of the DB gate, we have conducted quantum process tomography (QPT) and quantum state tomography (QST) experiments in three different environments: noiseless, noisy, and on IBM's real quantum computer. We have obtained results by repeating the quantum experiment for 4,000 shots for each measurement basis on the *ibm_oslo* machine, over all the 144 QPT circuits that were executed for the two-qubit DB gate. The final results for the 576 measurement outcomes over all circuits are used to rebuild the Choi matrices, which are then compared with the ideal expectations.

Our results demonstrate comparable fidelities from theoretical predictions and experimental settings, providing insights into implementations accuracy, measurement errors, and noise properties of the DB gate. Specifically, we have achieved a process fidelity of 0.8821327, 0.9707305 and 0.8069705 for the QPT experiments for the DB gate via a noisy simulation, noise-free environment, and on the IBM real machine *ibm_oslo*, respectively. The running time on the *ibm_oslo* quantum computer was 2 m and 43.5 s. Additionally, we have performed the QST experiments for 4,000 times in each setting, and obtained a state fidelity of 0.69365, 0.99269 and 0.88587, respectively. The running time on the *ibm_oslo* machine was 13.8 s. This study provides important insights into the performance of the DB gate on a NISQ device and demonstrate the potential of the two-qubit entangling gate for performing complex algorithms and operations on a genuine quantum computer.

CRediT authorship contribution statement

Muhammad AbuGhanem: Conceptualization, Data curation, Formal analysis, Investigation, Methodology, Resources, Software, Validation, Visualization, Writing – original draft, Writing – review & editing. **Hichem Eleuch:** Investigation, Validation, Writing – review & editing.

Declaration of competing interest

The authors declare that they have no known competing financial interests or personal relationships that could have appeared to influence the work reported in this paper.

Data availability

The data sets generated during and/or analyzed during the current study are included within this article.

Acknowledgments

We acknowledge the use of IBM Quantum for this research. The authors views and conclusions are their own, and they do not represent IBM Quantum's official policy or position. "This research received no specific grant from any funding agency in the public, commercial, or not-for-profit sectors."

References

[1] AbuGhanem M, Eleuch H. NISQ computers: a path to quantum supremacy. 2023, http://dx.doi.org/10.48550/arXiv.2310.01431, arXiv preprint arXiv:2310.01431 [quant-ph].
[2] Arute F, et al. Quantum supremacy using a programmable superconducting processor. Nature 2019;574:505–10.
[3] IBM Quantum. 2023, https://quantum-computing.ibm.com. [accessed].

[4] Underwood DL, Glick JA, Inoue K, et al. Using cryogenic CMOS control electronics to enable a two-qubit cross-resonance gate. 2023, arXiv:2302.11538 [quant-ph].
[5] Preskill John. Quantum computing in the NISQ era and beyond. Quantum 2018;2:79.
[6] Vidal G. Efficient classical simulation of slightly entangled quantum computations. Phys Rev Lett 2003;91:14.
[7] Gamel O. Entangled Bloch spheres: Bloch matrix and two-qubit state space. Phys Rev A 2016;93:062320.
[8] Hong Sabrina S, et al. Demonstration of a parametrically-activated entangling gate protected from flux noise. Phys Rev A 2020;101:012302.
[9] DiVincenzo DP. The physical implementation of quantum computation. Fortschr Phys 2000;48.
[10] Barenco A, Bennett CH, Cleve R, et al. Elementary gates for quantum computation. Phys Rev A 1995;52:3457.
[11] Fan YJ, Zheng Z-F, Zhang Y, et al. One-step implementation of a multi-target-qubit controlled phase gate with cat-state qubits in circuit QED. Front Phys 2019;14:21602.
[12] Li JF, Hu JR, Wan F, et al. Optimization two-qubit quantum gate by two optical control methods in molecular pendular states. Sci Rep 2022;12:14918.
[13] AbuGhanem M, Homid A, Abdel-Aty M. Cavity control as a new quantum algorithms implementation treatment. Front Phys 2018;13:1.
[14] Jiang Jehn-Ruey, Chu Chun-Wei. Classifying and benchmarking quantum annealing algorithms based on quadratic unconstrained binary optimization for solving np-hard problems. IEEE Access 2023;11:104165–78. http://dx.doi.org/10.1109/ACCESS.2023.3318206.
[15] Barone A, Paterno G. Physics and applications of the josephson effect. John Wiley and Sons; 1982.
[16] Fredkin E, Toffoli T. Conservative logic. Internat J Theoret Phys 1982;21.
[17] DiVincenzo DP. Quantum computation. Science 1995;270:5234.
[18] Kane B. A silicon-based nuclear spin quantum computer. Nature 1998;393:6681.
[19] Gershenfeld N, Chuang IL. Bulk spin resonance quantum computation. Science 1997;275:5298.
[20] Cory DG, Fahmy AF, Havel TF. Ensemble quantum computing by NMR spectroscopy. Proc Natl Acad Sci 1997;94:5.
[21] Nakamura Y, Pashkin YA, Tsai JS. Coherent control of macroscopic quantum states in a single-Cooper-pair box. Nature 1999;398.
[22] Platzman PM, Dykman MI. Quantum computing with electrons floating on liquid helium. Science 1999;284:5422.
[23] Steffen M, DiVincenzo DP, Chow JM, et al. Quantum computing: An IBM perspective. IBM J Res Dev 2011;55.
[24] Martinis JM. Superconducting phase qubits. Quant Inf Proc 2009;8:81–103.
[25] Devoret M, Wallraff A, Martinis J. Superconducting qubits: A short review. 2004, arXiv:cond-mat/0411174v1.
[26] Devoret MH, Martinis JM. Implementing qubits with superconducting integrated circuits. Quant Inf Proc 2004;3:163–203.
[27] Ladd TD, Jelezko F, Laflamme R, et al. Quantum computers. Nature 2010;464:45–53.
[28] Chow J, Gambetta J, Magesan E, et al. Implementing a strand of a scalable fault-tolerant quantum computing fabric. Nature Commun 2014;5:4015.
[29] Barends R, Kelly J, Megrant A, et al. Superconducting quantum circuits at the surface code threshold for fault tolerance. Nature 2014;508:500–3.
[30] Ladd TD, Jelezko F, Laflamme R, et al. Quantum computers. Nature 2010;464:45.
[31] Wang T, Zhang Z, Xiang L, et al. The experimental realization of high-fidelity shortcut-to-adiabaticity quantum gates in a superconducting Xmon qubit. New J Phys 2018;20:065003.
[32] Nielsen MA, Chuang IL. Quantum computation and quantum information. 10th anniversary ed. Cambridge: Cambridge University Press; 2011.
[33] Chuang I. Building the building blocks. Nat Phys 2018;14:974.
[34] Boudreault C, Eleuch H, Hilke M, Mackenzie R. Universal quantum computation with symmetric qubit clusters coupled to an environment. Phys Rev A 2022;106:062610.
[35] Bremner MJ, Dawson CM, Dodd JL, et al. Practical scheme for quantum computation with any two-qubit entangling gate. Phys Rev Lett 2002;89:247902.
[36] Lu Yao, Zhang S, Zhang K, et al. Global entangling gates on arbitrary ion qubits. Nature 2019;572.
[37] Koch J, Yu TM, Gambetta J, et al. Charge-insensitive qubit design derived from the Cooper pair box. Phys Rev A 2007;76:042319.
[38] Rigetti C, Devoret M. Fully microwave-tunable universal gates in superconducting qubits with linear couplings and fixed transition frequencies. Phys Rev B 2010;81:134507.
[39] Blais A, Gambetta J, Wallraff A, et al. Quantum information processing with circuit quantum electrodynamics. Phys Rev A 2007;75:032329.
[40] Rigetti C, Blais A, Devoret M. Protocol for universal gates in optimally biased superconducting qubits. Phys Rev Lett 2005;94:240502.
[41] Poletto S, Gambetta JM, Merkel ST, et al. Entanglement of two superconducting qubits in a waveguide cavity via monochromatic two-photon excitation. Phys Rev Lett 2012;109:240505.
[42] Leek PJ, Filipp S, Maurer P, et al. Using sideband transitions for two-qubit operations in superconducting circuits. Phys Rev B 2009;79:180511.
[43] Chow JM, Corcoles AD, Gambetta JM, Rigetti C, et al. Simple all-microwave entangling gate for fixed-frequency superconducting qubits. Phys Rev Lett 2011;107:080502.
[44] Sheldon S, Magesan E, Chow JM, Gambetta JM. Procedure for systematically tuning up cross-talk in the cross-resonance gate. Phys Rev A 2016;93:060302.
[45] DiCarlo L, Chow JM, Gambetta JM, et al. Demonstration of two-qubit algorithms with a superconducting quantum processor. Nature 2009;460:240.
[46] Reed M. Entanglement and quantum error correction with superconducting qubits [Ph.D. thesis], Yale; 2013.
[47] Yamamoto T, Neeley M, Lucero E, et al. Quantum process tomography of two-qubit controlled-Z and controlled-NOT gates using superconducting phase qubits. Phys Rev B 2010;82:184515.
[48] Hutchings MD, Hertzberg JB, et al. Tunable Superconducting qubits with flux-independent coherence. Phys Rev Appl 2017;8:044003.
[49] Strauch FW. Quantum logic gates for superconducting resonator qudits. Phys Rev A 2011;84:052313.
[50] Sete EA, Zeng WJ, Rigetti CT. 2016 IEEE international conference on rebooting computing. 2016.
[51] Kelly J, Barends R, Fowler AG, et al. State preservation by repetitive error detection in a superconducting quantum circuit. Nature 2015;519:66.
[52] Kerman AJ, Oliver WD. High-fidelity quantum operations on superconducting qubits in the presence of noise. Phys Rev Lett 2008;101:070501.
[53] Niskanen AO, Nakamura Y, Tsai JS. Tunable coupling scheme for flux qubits at the optimal point. Phys Rev B 2006;73:094506.
[54] Bertet P, Harmans CJPM, Mooij JE. Parametric coupling for superconducting qubits. Phys Rev B 2006;73:064512.
[55] Niskanen AO, Harrabi K, Yoshihara F, Nakamura Y, Lloyd S, Tsai JS. Quantum coherent tunable coupling of superconducting qubits. Science 2007;316:723.
[56] Naik RK, Leung N, Chakram S, et al. Random access quantum information processors. Nature Commun 2017;8:1904.
[57] Strand JD, Ware M, Beaudoin F, et al. First-order sideband transitions with flux-driven asymmetric transmon qubits. Phys Rev B 2013;87:220505.
[58] Beaudoin F, da Silva MP, Dutton Z, Blais A. First-order sidebands in circuit QED using qubit frequency modulation. Phys Rev A 2012;86:022305.
[59] Roy T, Kundu S, Ch M, et al. Implementation of pairwise longitudinal coupling in a three-qubit superconducting circuit. Phys Rev Appl 2017;7:054025.
[60] Royer B, Grimsmo AL, Didier N, Blais A. Fast and high-fidelity entangling gate through parametrically modulated longitudinal coupling. Quantum 2017;1:11.
[61] McKay DC, Filipp S, Mezzacapo A, et al. Universal gate for fixed-frequency qubits via a tunable bus. Phys Rev Appl 2016;6:064007.
[62] Bialczak RC, Ansmann M, Hofheinz M, et al. Quantum process tomography of a universal entangling gate implemented with Josephson phase qubits. Nat Phys 2010;6.
[63] Peterson EC, Crooks GE, Smith RS. Two-qubit circuit depth and the monodromy polytope. 2020, arXiv:[quant-ph] 1904.10541.
[64] McDermott R, Simmonds RW, Steffen M, et al. Simultaneous state measurement of coupled Josephson phase qubits. Science 2005;307:5713.
[65] Steffen M, Ansmann M, Bialczak RC, et al. Measurement of the entanglement of two superconducting qubits via state tomography. Science 2006;313:5792.
[66] Johnson PR, Strauch FW, Dragt AJ, et al. Spectroscopy of capacitively coupled josephson-junction qubits. Phys Rev B 2003;67(2):020509.
[67] Zeuch D, Hassler F, Slim J, DiVincenzo DP. Exact rotating wave approximation. 2018, arXiv:[quant-ph] 1807.02858.
[68] Kaye P, Laflamme R, Mosca M. An introduction to quantum computing. USA: Oxford University Press; 2007.
[69] Plantenberg JH, de Groot PC, Harmans CJPM, Mooij JE. Demonstration of controlled-NOT quantum gates on a pair of superconducting quantum bits. Nature 2007;447(7146):836–9.
[70] Schuch N, Siewert J. Natural two-qubit gate for quantum computation using the xy interaction. Phys Rev A 2003;67(3):032301.
[71] Yamamoto T, Pashkin Y, Astafiev O, Nakamura Y, Tsai JS. Demonstration of conditional gate operation using superconducting charge qubits. Nature 2003;425(6961):941–4.
[72] Zanardi P, Zalka C, Faoro L. Entangling power of quantum evolutions. Phys Rev A 2000;62:30301(R).
[73] Caldwell SA, Didier N, Ryan CA, et al. Parametrically activated entangling gates using Transmon qubits. Phys Rev Appl 2018;10:034050.
[74] Horodecki M, Horodecki P, Horodecki R. General teleportation channel, singlet fraction, and quasidistillation. Phys Rev A 1999;60:1888.
[75] Nielsen MA. A simple formula for the average gate fidelity of a quantum dynamical operation. Phys Lett A 2002;303:249.
[76] Zhang J, Souza AM, Brandao FD, Suter D. Protected quantum computing: Interleaving gate operations with dynamical decoupling sequences. Phys Rev Lett 2014;112:050502.
[77] Choi MD. Completely positive linear maps on complex matrices. Linear Algebra Appl 1975;10:285.
[78] Jamiołkowski A. Linear transformations which preserve trace and positive semidefiniteness of operators. Rep Math Phys 1972;3:275.
[79] Kraus K. States, effects, and operations. Berlin: Springer-Verlag; 1983.

[80] Chuang IL, Nielsen MA. Prescription for experimental determination of the dynamics of a quantum black box. J Modern Opt 1997;44:2455.
[81] Poyatos J, Cirac JI, Zoller P. Complete characterization of a quantum process: the two-bit quantum gate. Phys Rev Lett 1997;78:390.
[82] Mitchell MW, et al. Diagnosis, prescription, and prognosis of a Bell-State filter by quantum process tomography. Phys Rev Lett 2003;91:120402.
[83] O'Brien JL, et al. Quantum process tomography of a controlled-not gate. Phys Rev Lett 2004;93:080502.
[84] Lehnert KW, et al. Measurement of the excited-state lifetime of a microelectronic circuit. Phys Rev Lett 2003;90:027002.
[85] AbuGhanem M, Eleuch H. Experimental characterization of Google's sycamore quantum AI on an IBM's quantum computer. 2023, http://dx.doi.org/10.2139/ssrn.4299338, SSRN.
[86] AbuGhanem M, Eleuch H. Full quantum state tomography study of Google's sycamore gate on an IBM's quantum computer. 2023, http://dx.doi.org/10.2139/ssrn.4316581, SSRN.
[87] AbuGhanem M, Eleuch Hichem. Quantum tomography study of DB Gate on an IBM's quantum computer. 2023, http://dx.doi.org/10.2139/ssrn.4262095, SSRN.
[88] James DF, Kwiat PG, Munro WJ, White AG. On the measurement of qubits. Phys Rev A 2001;64:052312.
[89] Teo YS, et al. Quantum-state reconstruction by maximizing likelihood and entropy. Phys Rev Lett 2011;107:020404.
[90] Smolin JA, Gambetta JM, Smith G. Efficient method for computing the maximum-likelihood quantum state from measurements with additive Gaussian noise. Phys Rev Lett 2012;108:070502.
[91] Qi B, et al. Adaptive quantum state tomography via linear regression estimation: Theory and two-qubit experiment. npj Quantum Inf 2017;3.
[92] Bolduc E, Knee GC, Gauger EM, Leach J. Projected gradient descent algorithms for quantum state tomography. npj Quantum Inf 2017;3.
[93] Qiskit. 2023, http://www.qiskit.org. [Accessed].